



**HAL**  
open science

# Modeling of large-scale under-expanded hydrogen jet fires

Jean-Louis Consalvi, Fatiha Nmira

► **To cite this version:**

Jean-Louis Consalvi, Fatiha Nmira. Modeling of large-scale under-expanded hydrogen jet fires. Proceedings of the Combustion Institute, 2019, 37 (3), pp.3943-3950. hal-01990517

**HAL Id: hal-01990517**

**<https://hal.science/hal-01990517>**

Submitted on 21 Oct 2021

**HAL** is a multi-disciplinary open access archive for the deposit and dissemination of scientific research documents, whether they are published or not. The documents may come from teaching and research institutions in France or abroad, or from public or private research centers.

L'archive ouverte pluridisciplinaire **HAL**, est destinée au dépôt et à la diffusion de documents scientifiques de niveau recherche, publiés ou non, émanant des établissements d'enseignement et de recherche français ou étrangers, des laboratoires publics ou privés.



Distributed under a Creative Commons Attribution - NonCommercial 4.0 International License

## Modeling large-scale under-expanded hydrogen jet fires

Jean-Louis Consalvi<sup>\*,†</sup>, Fatiha Nmira<sup>\*\*</sup>

<sup>\*</sup>Aix-Marseille Université, CNRS, IUSTI UMR 7343, 5 rue E. Fermi, 13013 Marseille, France.

<sup>\*\*</sup> Direction R&D EDF, 6 quai Watier, 78400 Chatou, France.

<sup>†</sup> Corresponding author. Fax: (+33)491106969. Email: jean-louis.consalvi@univ-amu.fr

<b>Name of Colloquium:</b>	<b>Fire research</b>
<b>Estimate of total length:</b>	<b>6001 words</b>
<b>Method of determination:</b>	<b>Method 1, Word users</b>
<b>Main text:</b>	<b>3276 words</b>
<b>Equations:</b>	<b>91.2 words</b>
Eqs. 1-4 (1equation lines + 2blank lines) x (7.6 words/line) x (1columns): 22.8 words	
<b>References:</b>	<b>(25 references + 2) x (2.3 lines/reference) x (7.6 words/line) : 471.96 words</b>
<b>Tables and captions:</b>	<b>458.7 words</b>
Table 1: Word count = (14 text lines + 2 lines) x (7.6 words/line) x (2columns) + (21words in caption): 264.2 words	
Table 2: Word count = (22 text lines + 2 lines) x (7.6 words/line) x (1columns) + (12words in caption): 194.4	
<b>Figures and captions:</b>	<b>1703.12 words</b>
Fig. 1: (53.6 mm + 10 mm)x(2.2 words/mm)x(1columns) + (20words in caption): 159.92 words	
Fig. 2: (107.2 mm + 10 mm)x(2.2 words/mm)x(2columns)+(47words in caption): 562.68 words	
Fig. 3: (53.6 mm + 10 mm)x(2.2 words/mm)x(1columns) + (32words in caption): 171.92 words	
Fig. 4: (53.6 mm + 10 mm)x(2.2 words/mm)x(1columns) + (30words in caption): 162.92 words	
Fig. 5: (53.6 mm + 10 mm)x(2.2 words/mm)x(1columns) + (33words in caption): 172.92 words	
Fig. 6: (53.6 mm + 10 mm)x(2.2 words/mm)x(1columns) + (15words in caption): 154.92 words	
Fig. 7: (53.6 mm + 10 mm)x(2.2 words/mm)x(1columns) + (15words in caption): 154.92 words	
Fig. 8: (53.6 mm + 10 mm)x(2.2 words/mm)x(1columns) + (16words in caption): 155.92 words	

words

I agree to pay color reproduction charges if applicable.

# Modeling of large-scale under-expanded hydrogen jet fires

Jean-Louis Consalvi<sup>\*,†</sup>, Fatiha Nmira<sup>\*\*</sup>

\*Aix-Marseille Université, CNRS, IUSTI UMR 7343, 5 rue E. Fermi, 13013 Marseille, France.

\*\* Direction R&D EDF, 6 quai Watier, 78400 Chatou, France.

**Abstract :** Large-scale hydrogen under-expanded jet flames and lab-scale H<sub>2</sub> and CH<sub>4</sub> jet flames are simulated by using the standard k-ε model coupled to a hybrid flamelet/transported PDF method and a narrow band correlated-k gas radiation model. The set of flames considered covers a wide range of residence times and optical thicknesses. The notional nozzle concept is adopted to determine injection conditions for the large-scale choked flames. Model predictions in terms of flame geometry, flame structure, radiant fraction and radiative flux are consistent with the experimental data whatever the scales. Model results show that these flames do not verify the optically-thin approximation since the part of emitted radiant power re-absorbed within the flame ranges from 11% for the smallest H<sub>2</sub> flame to about 70% for the largest H<sub>2</sub> flame. Neglecting the turbulence-radiation interaction underestimates significantly the radiant fraction whatever the scale and these discrepancies are enhanced with increasing residence time and optical thickness. A simple analysis based on the assumption of homogenous flame is used to correlate the experimental radiant fraction as a function of  $\tau_G E_m (1 - \dot{Q}_{abs}/\dot{Q}_{em})$  where  $\tau_G$ ,  $E_m$  and  $\dot{Q}_{abs}/\dot{Q}_{em}$  represent the residence time, an equivalent emission term and the part of emitted radiant power re-absorbed within the flame. Model results are used to provide a proper estimation of the equivalent emission term and self-absorption.

**Key Words:** Under-expanded H<sub>2</sub> flames, lab-scale CH<sub>4</sub> and H<sub>2</sub> flames, transported PDF method, narrow-band correlated-k model, radiant fraction, turbulence-radiation interaction.

## 1. Introduction

Large-scale jet fires resulting from the ignition of hydrogen released from a sudden leak in high-pressure hydrogen-storage tanks represent a realistic safety scenario. For this scenario gas radiation is the primary mode of heat transfer and, as such, focuses the attention.

Schefer et al. [1, 2] provided experimental investigations of this scenario by characterizing the geometry and the radiative characteristics of large-scale vertical subsonic and sonic (choked) hydrogen-jet flames. They demonstrated that correlations and scaling relationships for flame length and width, and radiative outputs, established for smaller-scale flames, can be extended to large-scale jet fires. For choked jets, the notional nozzle concept, proposed by Birch et al. [3], was introduced to account for the sudden expansion of the high-pressure jet fluid to atmospheric pressure. Molina et al. [4] used these data along with lab-scale experimental data obtained for non-sooting hydrocarbons to provide a correlation relating the radiant fraction to the residence time (as defined by Turns and Myhr [5]) multiplied by an emission term characterizing the fuel. This correlation revealed that the radiant fractions of the large-scale jet flames were smaller than those predicted by the correlation for lab-scale flames. These discrepancies were attributed to the optically-thin approximation, used to establish the correlation that should cease to be valid for large-scale flames.

The development of accurate high-temperature spectroscopic databases, such as HITEMP 2010 [6], and gas radiative property models based on the k-distribution concept [7] allowed to provide reliable calculations of gas radiation in combustion systems. These scheme coupled to transported PDF methods to describe accurately the Turbulence-Radiation Interaction (TRI) provided accurate predictions of radiative heat transfer in both non-luminous and luminous lab-scale jet flames [7-9]. However, to the authors' best knowledge such advanced radiation models were not applied to large-scale hydrogen jet fires, the previous modeling studies

focusing on the flame geometry [10] or having used old version of the weighted-sum-of grey-gases [11].

The first objective of this article is to simulate the high-pressure under-expanded hydrogen-jet flames investigated experimentally by Schefer et al. [2] by using a Narrow Band Correlated-k (NBCK) method coupled to a transported PDF approach to model emission TRI. In addition, lab-scale experiments of hydrogen and methane jet flames [1, 2] will be also simulated. Model results will be compared systematically with available experimental data and used to provide a better understanding of the radiative structure of these flames.

## 2. Numerical model

The turbulent jet diffusion flames are modelled by using the physical models and numerical algorithms described in details in Refs [8, 9].

### 2.1. Turbulent combustion and soot production

The Favre-Averaged Navier-Stokes equations are solved in axisymmetric cylindrical coordinates in connection with the k- $\epsilon$  model with the standard set of constants, except  $C_{\epsilon 1}$  that was set equal to 1.5. The use of this value rather than the standard value of 1.44 was found to match the experimental data better in lab-scale flames [7]. The enthalpy defect flamelet model is used to obtain state relationships for density, species and temperature as unique functions of mixture fraction,  $\zeta$ , scalar dissipation rate,  $\chi$ , and enthalpy defect,  $h - h_{ad}$  where  $h_{ad}$  is the adiabatic enthalpy [8, 9]. The flamelet library was generated by using the mechanism of hydrogen oxidation developed by Burke et al. [12]. For the lab-scale methane flames, as in previous studies [8, 9], the mechanism of Qin et al. [13] and the acetylene/benzene-based two-equation soot model, proposed by Lindstedt [14], were used.

## 2.2. Radiation model

The spectral coverage range in terms of wavenumber (inverse of the wavelength),  $\eta$ , is 12.5-11262.5  $\text{cm}^{-1}$  and  $\text{H}_2\text{O}$  is considered as radiative participating species. The contribution of  $\text{CO}_2$  and soot are also considered in the methane flames with the Rayleigh's theory being applied to obtain the soot absorption coefficient [8, 9]. Spectral gas radiation was modelled using the optimized NBCK model with 52 Narrow Bands (NB) described in Ref. [15]. A database of mixed NB k-g distributions was generated from HITEMP 2010 [6] and by using the mixing scheme of Modest and Riazzi [16]. For each NB, mixed k-g distributions were stored at the 10 Gauss points used to solve the NB Radiative Transfer Equation (RTE) (Eq. 1), for 6 mole fractions of  $\text{CO}_2$  and  $\text{H}_2\text{O}$  ranging between 0 and 1 (0, 0.1, 0.25, 0.5, 0.75, 1) and for 38 temperatures ranging from 300 to 4000 K (by step of 100 K). At each grid node and for each NB (index  $i$ ) and Gauss point (index  $k$ ), the absorption coefficient,  $k_k^i$ , required to solve the NB RTE is extracted from the database by using linear interpolations on  $x_{\text{CO}_2}$  and  $x_{\text{H}_2\text{O}}$  and a spline interpolation on  $T$ . In sooting methane flames, the soot absorption coefficient, evaluated at the center of the narrow band,  $\eta_i$ , is added to  $k_k^i$ . The Reynolds-averaged NB RTE is given by:

$$\frac{d}{ds} \langle I_k^i \rangle + \langle k_k^i \rangle \langle I_k^i \rangle = \langle k_k^i I_{b\eta,i} \rangle \quad (1)$$

where the spectral blackbody intensity,  $I_{b\eta,i}$ , is evaluated at the center of the NB and the brackets denotes Reynolds averaging. The NB model was found to provide spectrally-integrated quantities in very good accordance with those obtained with line-by-line models [15]. The NB RTE is solved by using the Finite Volume Method [17] with a  $12 \times 16$  angular discretization. Absorption TRI,  $\langle k_k^i I_k^i \rangle$ , is modeled by using the optically-thin fluctuation approximation (OTFA), assuming that the absorption coefficient and the radiative intensity

are weakly correlated. This implies that  $\langle k_k^i I_k^i \rangle = \langle k_k^i \rangle \langle I_k^i \rangle + \langle k_k^{i'} I_k^{i'} \rangle \approx \langle k_k^i \rangle \langle I_k^i \rangle$  where  $\phi'$  denotes the Reynolds fluctuation of the variable  $\phi$ . This approximation was found to be valid for laboratory-scale and large-scale sooting jet flames [7, 18]. Its validity for the present flames was verified *a posteriori* by using the stochastic time and space series described in Ref. [18]. Emission TRI,  $\langle k_k^i(x_i, T) I_{b\eta, i}(T) \rangle$ , depends only on local quantities and can be modelled exactly by using a one-point, one-time composition PDF [7].

### 2.3. Transported PDF method

Based on previous studies, the scalar dissipation rate is assumed to be statistically independent of the other scalars and its PDF is modelled by a Dirac function [8, 9]. The default set of composition variables is therefore  $\underline{\phi} = \{\zeta, X_R\}$  ( $= \{\zeta, X_R, N_S, Y_S\}$  in the case of methane flame with  $N_S$  and  $Y_S$  being the soot number density and mass fraction). A gradient transport model for turbulent velocity fluctuations and the Interaction by Exchange with the Mean (IEM) model are considered to close both turbulent diffusion and micro-mixing terms [8, 9]. The apparent turbulent Prandtl number and the constant  $C_\phi$  were set equal to 0.7 and 2.0, respectively. The joint composition PDF transport is solved using the Stochastic Eulerian Field method [19].

## 3. Results and discussions

### 3.1. Experimental data and computational details

The large-scale vertical hydrogen-jet flames, investigated experimentally by Schefer et al. [2], were simulated. Hydrogen was released from high-pressure storage tubes with a pressure decreasing exponentially from its initial value of 413 bar to near atmospheric pressure over a period of approximately 500 s. The inner diameter of the jet,  $d_j$ , was 5.08 mm. At these pressures the flows exiting the jet nozzle are categorized as under-expanded jets in which the

flow is choked at the jet exit and the exit pressure is considerably greater than atmospheric pressure. The flow rapidly accelerates and expands to atmospheric pressure through a series of expansion shocks. Table 1 shows the exit velocity,  $U_j$ , and temperature,  $T_j$ , at different times during the experiments. These data were determined from measured conditions in the reservoir by applying isentropic flow relations and assuming that the gas follows the Noble-Abel equation of state [2]. More details can be found in Ref. [2]. In order to avoid complexity related to the modeling of the expansion, the concept of notional nozzle, proposed by Birch et al. [3], is used. The notional nozzle concept was applied with success in previous numerical modeling studies of large-scale under-expanded hydrogen flames [10, 11], leading to predictions of flame geometry consistent with experimental data. It considers mass and momentum conservations to determine effective conditions in terms of diameter,  $d_{eff}$ , velocity,  $V_{eff}$ , and temperature,  $T_{eff}$ , which are used as injection conditions after the expansion. The values of  $d_{eff}$ ,  $V_{eff}$  and  $T_{eff}$  used in the present simulations are also reported in Table 1. The lab-scale subsonic H<sub>2</sub> and CH<sub>4</sub> flames reported in Refs. [1, 2, 20, 21] were also simulated. Injection conditions for these flames are also summarized in Table 1. The sixth column represents the fuel flow rate. The penultimate column of Table 1 corresponds to the chemical heat release rate,  $\dot{Q}_c$ .

**Table 1.** Flame conditions. For the large-scale H<sub>2</sub> flames, the values in parenthesis are relative to injection through the notional nozzle.

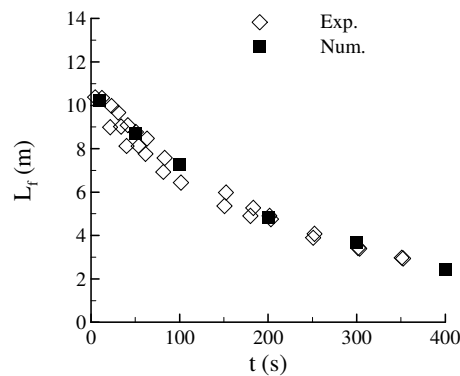
Flame n°	$t$ (s)	$d_j$ ( $d_{eff}$ ) (mm)	$U_j$ ( $V_{eff}$ ) (m/s)	$T_j$ ( $T_{eff}$ ) (K)	$\dot{m}_F$ (g/s)	$\dot{Q}_c$ (kW)	Ref.
Large-Scale H <sub>2</sub> flame							
1	10	5.08 (51.5)	1259 (2047)	214 (268)	359.3	46310	[2]
2	50	5.08 (39.6)	1154 (1906)	196 (242)	228.6	28212	-
3	100	5.08 (31.0)	1101 (1834)	189 (231)	142.6	17417	-
4	200	5.08 (20.5)	1071 (1786)	190 (229)	64.2	7514	-
5	300	5.08 (13.6)	1066 (1743)	193 (232)	28.2	3156	-
6	400	5.08 (8.6)	1069 (1622)	196 (236)	11.2	1172	-
Lab-Scale H <sub>2</sub> flames							
7-11		1.91	87.7-349	300	0.021-0.083	2.64-10	[1]
12		3.75	296	300	0.276	33.2	[20,21]

Lab-Scale CH <sub>4</sub> flames							
13-16		1.91	58.2-116.6	300	0.11-0.222	5.54-11.08	[2]

For the lab-scale flames, a computational domain with a size of 0.1m (r) × 1m (z) was used. In these cases a non-uniform mesh of 54 (r) × 93 (z) was found to be sufficient to achieve an independent grid solution. For the large-scale flames, the computational domain and the mesh were specific for each case. For these cases, a uniform mesh was used in the flaming region with a grid size of 2cm × 2cm.

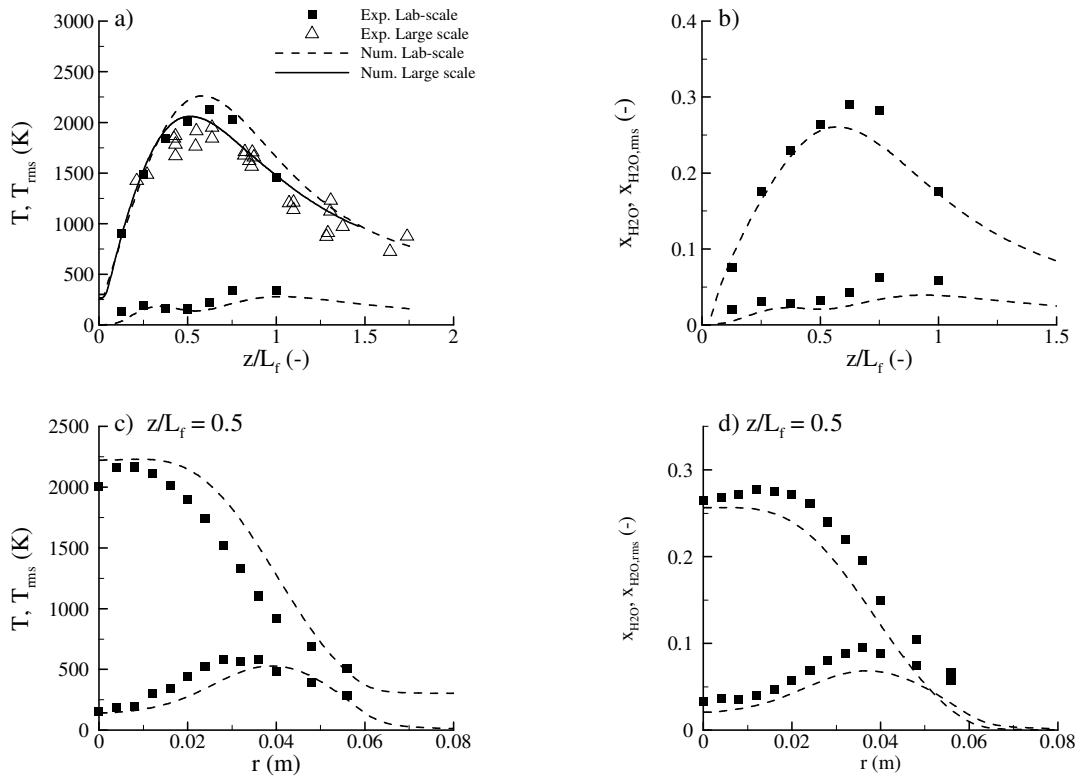
### 3.2. Comparison with experimental data

Analysis of the experimental axial profiles of mean temperature for hydrogen lab-scale [20] and large-scale [22] flames shows that the measurements of visible flame length corresponds to a range of temperature between 1330 K and 1660 K, approximately. Consistently the numerical flame length is defined by the isotherm 1500 K. Figure 1 shows that the model reproduces well the time evolution of the visible flame length reported by Schefer et al. [2] for large-scale under-expanded jet fires.



**Figure 1.** Large-scale flame length as a function of time. The experimental data are taken from Schefer et al. [2].

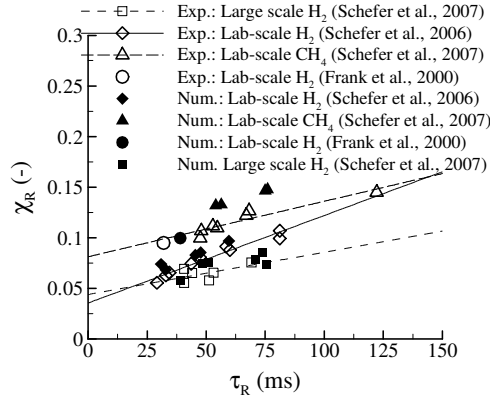
Figure 2 displays both predicted and measured axial and radial distributions of the mean and rms values of temperature and H<sub>2</sub>O mole fraction for the lab-scale H<sub>2</sub> flames of Barlow and Carter [20]. These quantities are well predicted by the numerical model. Axial profiles of mean temperature for hydrogen large-scale flames, measured by Schefer et al. [1] and reported by Houf et al. [22], are also plotted in Fig. 2a along with the simulation of the large-scale flame at  $t = 10$  s (see Table 1). The predicted axial profiles for the other large-scale jet flames in Table 1 are similar and are not plotted in Fig. 2a to avoid overloading the figure. Measured and predicted axial profiles of temperature for large-scale flames compare favorably and are in good accordance with those of lab-scale flames despite lower temperature peaks. It should be pointed out that the comparison for large-scale flames is only qualitative since experiments are relative to the conditions reported in Ref. [1] and the simulations correspond to the conditions reported in Ref. [2].



**Figure 2.** Axial and radial profiles of mean and fluctuation of temperature and H<sub>2</sub>O mole fraction. Lab-scale experimental data are taken from Barlow et al. [20] whereas large-scale

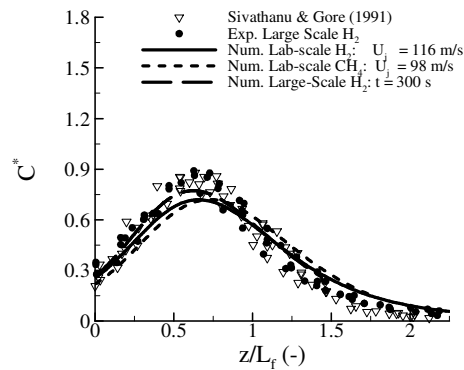
experimental data are taken from the experiments of Schefer et al. [1] as reported by Houf et al. [22].

Figure 3 displays the radiant fraction,  $\chi_R = (\dot{Q}_{em} - \dot{Q}_{abs})/\dot{Q}_c$ , as a function of the residence time,  $\tau_G = \rho_f W_f^2 L_f f_s / 3 \rho_j d_j^2 U_j$ , defined by Turns and Mhyr [5].  $\dot{Q}_{em} = \int_{V_f} \int_{\eta} 4\pi \langle \kappa_{\eta} I_{b\eta} \rangle \kappa_{\eta} d\eta dV$  is the total emission with  $V_f$  and  $\kappa_{\eta}$  being the flame volume and the spectral absorption coefficient.  $\dot{Q}_{abs} = \int_{V_f} \int_{\eta} \langle \kappa_{\eta} \rangle \langle G_{\eta} \rangle d\eta dV$  is the total absorption with  $G_{\eta}$  being the spectral incident radiation.  $\rho_f$ ,  $W_f$ , and  $f_s$  are the density of the mixture of the products of a stoichiometric flame, the flame width, and the mass fraction of fuel at stoichiometric conditions, respectively. Schefer et al. [1, 2] showed that the relationship between flame width and length,  $W_f = 0.17L_f$ , established by Turns and Mhyr [5] for lab-scale jet flames, can also be applied for large-scale jet flames. This relationship is also used to compute numerical residence times. For lab-scale methane flames, the peak of soot volume fraction ranges from 0.01 ppm for the  $U_j = 116$  m/s flame to 0.02 ppm for the  $U_j = 58$  m/s. For these levels, the contribution of soot to radiative heat transfer is negligible. Figure 3 shows that, for a given set of experiments, the radiant fraction increases linearly with the residence time. For a given residence time, the radiant fraction is higher for the lab-scale CH<sub>4</sub> flames than for the lab-scale H<sub>2</sub> flames owing to a higher emission [4]. Radiant fractions for large-scale H<sub>2</sub> flames are lower than those of lab-scale H<sub>2</sub> flames which can be attributed, at least partially, to higher self-absorption [4]. It can be also observed in Fig. 3 that the radiant fraction for the lab-scale H<sub>2</sub> flame of Barlow et al. [21] is higher than the radiant fraction of other H<sub>2</sub> lab-scale flames with similar residence times. This point will be discussed in section 3.4. Model calculations follow these trends and are on the whole within 20% of the experiments.



**Figure 3.** Radiant fraction as a function of the residence time. The experimental data are taken from Barlow et al. [21] ( $\circ$ ), Schefer et al. [1] ( $\diamond$ ), and [2] ( $\square$  and  $\Delta$ ).

Figure 4 represents the non-dimensional radiative flux,  $C^* = 4\pi R^2 \dot{q}_R''(R, z) / (\chi_R \dot{Q}_C)$ , at a radial distance  $R = L_f/2$  from the burner axis, as a function of the height normalized by the visible flame length. This normalization, proposed by Sivathanu and Gore [23], allows the collapsing of experimental radiative flux onto a single curve independently of fuels, heat release rates and scales. Predicted radiative flux for lab-scale and large-scale  $H_2$  and lab-scale  $CH_4$  flames are also correlated when using this normalization. Computed normalized profiles are in good agreement with the experimental ones despite slight underestimation at the peak and overestimation for  $z/L_f$  higher than 1.5.



**Figure 4.** Normalized radiative flux at a distance  $R = L_f/2$  as a function of  $z/L_f$ . The experimental data are taken from Sivathanu and Gore [23] and Schefer et al. [1, 2].

### 3.3. Turbulence-radiation interaction

This section investigates the effects of TRI on the predicted radiant fractions. When TRI is disregarded (NoTRI), both total emission and absorption terms are simply evaluated based on mean species mole fraction and mean temperature, i.e.  $\dot{Q}_{em,NoTRI} = \int_{V_f} \int_{\eta} 4\pi\kappa_{\eta}(\langle x_i \rangle, \langle T \rangle) I_{b\eta}(\langle T \rangle) d\eta dV$  and  $\dot{Q}_{abs,NoTRI} = \int_{V_f} \int_{\eta} \kappa_{\eta}(\langle x_i \rangle, \langle T \rangle) \langle G_{\eta} \rangle d\eta dV$ . The use of coupled flow/turbulence/combustion/radiation computations to evaluate the role of TRIs can be misleading since the output variables of the radiative models are highly dependent on these strong couplings. The importance of TRIs can thus be better understood by considering decoupled radiation calculations. As a consequence,  $\dot{Q}_{em,NoTRI}$  and  $\dot{Q}_{abs,NoTRI}$ , used to compute the radiant fraction without TRI, were determined from decoupled radiation calculation by using mean properties computed with the complete CFD simulation (including TRI).

Figure 5 shows the ratio between the radiant fraction computed by taking TRI into account,  $\chi_{R,TRI}$ , to the radiant fraction computed by neglecting TRI,  $\chi_{R,NoTRI}$ .  $\chi_{R,TRI}/\chi_{R,NoTRI}$  ranges from 1.81 to 2.27, evidencing the importance of TRI on radiative outputs. The enhancement in radiant fraction due to TRI is higher than that reported in some previous studies (see Ref. [24] for example). However these studies, contrary to the present, have considered coupled flow/turbulence/combustion/radiation computations which tend to lower the influence of TRI and explains, at least partially, these differences.

Previous studies concerning non-luminous flames suggested that TRI effects increase with the optical thickness [24].  $\dot{Q}_{abs}/\dot{Q}_{em}$  quantifies the flame self-absorption and is used here as a measure of the optical thickness. Figure 5 confirms that TRI effects are enhanced by

increasing the optical thickness. It also shows that TRI effects are enhanced by increasing the residence time.

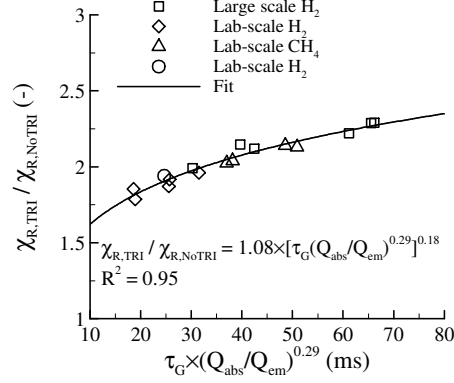


**Figure 5.** Effects of TRI on radiant fraction. Data are relative to the simulations of the experiments of Barlow et al. [21] ( $\circ$ ), Schefer et al. [1] ( $\diamond$ ), and [2] ( $\square$  and  $\Delta$ ).

### 3.4. Correlation for radiant fraction

The radiant fraction can be rewritten as:

$$\chi_R = \frac{\dot{Q}_{em}}{\dot{Q}_c} \left(1 - \frac{\dot{Q}_{abs}}{\dot{Q}_{em}}\right) = \chi_{em} \left(1 - \frac{\dot{Q}_{abs}}{\dot{Q}_{em}}\right) \quad (2)$$

where  $\chi_{em}$  represents the ratio of the heat release rate emitted in the flame to the chemical heat release rate.

Assuming a homogeneous flame,  $\chi_{em}$  can be related to the residence time multiplied by a characteristic emission term [4]:

$$\chi_{em} \propto \beta = \tau_G E_m = \tau_G \kappa_{p,em} T_{em}^4 \quad (3)$$

where  $E_m$  is the characteristic emission term and  $\kappa_{p,em}$  and  $T_{em}$  are characteristic Planck-mean absorption coefficient and flame radiation temperature. Molina et al. [4] assumed that the characteristic emission term is a fuel property and used the flame adiabatic temperature

(2390 K for H<sub>2</sub> and ~2250 K for CH<sub>4</sub>) as flame radiation temperature. In addition,  $\kappa_{p,em}$  was computed from RADCAL based on an equilibrium composition, leading to 0.23 m<sup>-1</sup> for H<sub>2</sub> and 0.5 m<sup>-1</sup> for CH<sub>4</sub> [4]. Nevertheless, it is recognized that flame radiation temperature is considerably lower than the flame adiabatic temperature and may also depend on the flame configuration [25]. The emission of an equivalent homogeneous medium can be defined properly by reproducing the emission of the medium:

$$E_{em,ref} = \frac{\dot{Q}_{em}}{4\sigma V_f} \quad (4)$$

where  $\sigma$  is the Stefan-Boltzmann constant. It should be pointed out that this definition of  $E_{em}$  includes the effects of flame optical thickness and TRI. Figure 6 confirms that the  $\chi_{em} \propto \beta$  provided that a realistic emission term is used. Table 2 shows that the emission fraction is influenced by both residence time and optical thickness. For a given set of experiments, the emission fraction increases on the whole with the residence time. The emission fraction of the largest H<sub>2</sub> flames (t = 10 s and 50 s) are the highest owing to their high optical thickness. The enhancement of emission due to CO<sub>2</sub> explains that the lab-scale CH<sub>4</sub> flames exhibit emission fraction comparable to the large-scale H<sub>2</sub> flames at t = 100 s and 200 s and higher than the other H<sub>2</sub> flames. Finally, the emission fraction of the lab-scale H<sub>2</sub> flame investigated by Barlow et al. [20, 21] has a higher emission fraction as compared to other lab-scale H<sub>2</sub> flames with similar residence times. This explains that it presents a higher radiant fraction than the other lab-scale H<sub>2</sub> flames in Fig. 3.

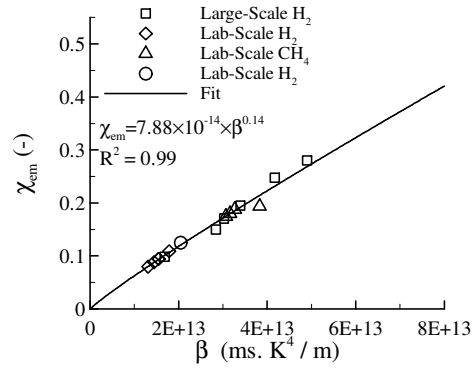


**Figure 6.** Computed  $\chi_{em}$  as a function of  $\beta = \tau_G E_{m,ref}$ . Same legend as in Fig. 5.

**Table 2.** Emission and radiant fractions of the computed flames.

n°	$\tau_G$ (ms)	$\frac{\dot{Q}_{abs}}{\dot{Q}_{em}}$	$\chi_{em}$ (-)	$\chi_R$ (-)
Large-Scale H <sub>2</sub> flame [2]				
1	74	0.65	0.248	0.085
2	75	0.64	0.280	0.073
3	71	0.60	0.195	0.078
4	48	0.50	0.171	0.074
5	51	0.53	0.150	0.075
6	39	0.41	0.099	0.058
Lab-Scale H <sub>2</sub> flames [1]				
7	60	0.11	0.109	0.097
8	48	0.12	0.095	0.083
9	45	0.14	0.095	0.081
10	33	0.15	0.080	0.068
11	31	0.17	0.088	0.073
Lab-Scale H <sub>2</sub> flames [21]				
12	39	0.20	0.125	0.099
Lab-Scale CH <sub>4</sub> flames [2]				
13	76	0.21	0.188	0.148
14	75	0.26	0.194	0.147
15	55	0.24	0.174	0.132
16	56	0.26	0.180	0.133

As expected from a simple analysis based on homogeneous and isotropic grey medium, Fig. 7 shows that  $\dot{Q}_{abs}/\dot{Q}_{em} \propto \kappa_{p,em} W_f \cdot \kappa_{p,em}$  was evaluated as proposed by Molina et al. [4], i.e. by assuming an adiabatic flame temperature and an equilibrium composition. The values of  $\kappa_{p,em}$  proposed by Molina et al. [4] were considered since they are in close agreement with those computed from HITEMP 2010 [6]. Figure 7 shows also that none of the flames can be considered as optically-thin since the part of the emitted radiative power re-absorbed within the flame ranges from about 11% for the smallest lab-scale H<sub>2</sub> flame to about 70% for the largest H<sub>2</sub> flame. Results in Fig. 7 show that the self-absorption is larger for the large-scale H<sub>2</sub> flames, followed by the lab-scale CH<sub>4</sub> flames and, finally, the labs-scale H<sub>2</sub> flames.

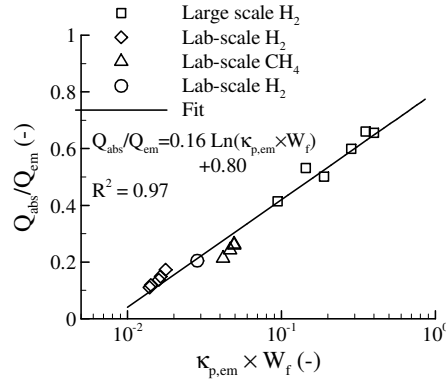


**Figure 7.** Computed  $\dot{Q}_{abs}/\dot{Q}_{em}$  as a function of  $\kappa_{p,ref}W_f$ . Same legend as in Fig. 5.

Figure 8 shows  $\chi_R$  as a function of  $\gamma = \tau_G E_{em,ref}(1 - \dot{Q}_{abs}/\dot{Q}_{em})$  for all the experimental data reported in Fig. 3. Both  $\dot{Q}_{abs}/\dot{Q}_{em}$  and  $E_{em,ref}$  were taken from the numerical simulations. These results show that the radiant for both lab-scale and large-scale flames can be correlated by using a simple homogenous flame analysis provided that a proper equivalent emission term is defined and self-absorption is taken into account. The dashed line, denoted as correlations in the legend of Fig. 8, represents  $\chi_R$  computed from Eq. 2 with the correlation of Fig. 6 for  $\chi_{em}$  and the correlation of Fig. 7 for  $\dot{Q}_{abs}/\dot{Q}_{em}$ . A good agreement is obtained as compared to the best fit.

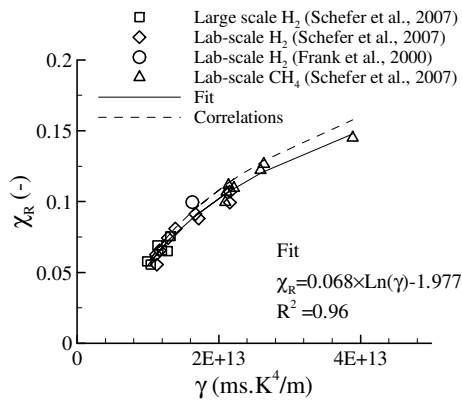


**Figure 8.** Experimental radiant fraction as a function of  $\gamma$ . Same legend as in Fig. 5.

#### 4. Conclusions

Large-scale H<sub>2</sub> under-expanded jet flames and lab-scale H<sub>2</sub> and CH<sub>4</sub> jet flames were simulated by using a k-ε model coupled to a hybrid flamelet/transported PDF method and a NBCK gas radiation model. The following conclusions can be drawn:

- 1) Model results are in good agreement with the available experimental data whatever the scale considered.
- 2) None of the flames considered can be assumed to be optically-thin since self-absorption represents at least 11% of the total emission.
- 3) Absorption TRI can be modeled by using the OTFA.
- 4) TRI enhances significantly the radiant fraction whatever the scale considered. This enhancement increases with both residence time and optical thickness and, as a result, is on the whole higher for large-scale H<sub>2</sub> flames and lab-scale CH<sub>4</sub> flames.
- 5) The emission fraction increases with both residence time and optical thickness and can be correlated with the product between the residence time and an equivalent emission term,  $\tau_G E_m$ , provided that a realistic emission term is considered.
- 6) Computed optical thicknesses, defined as the ratio of total absorption to total emission, are found to correlate with the Planck-mean absorption coefficient, evaluated based on an adiabatic flame temperature and an equilibrium composition, and the flame width.
- 7) Experimental radiant fraction for ‘non-luminous’ jet flames are found to correlate with the residence time, an equivalent emission term and the part of emitted radiant power re-absorbed within the flame whatever the scale considered.

## References

- [1]. R.W. Schefer, W.G. Houf, B. Bourne, J. Colton, Int. J. Hydrogen Energ. 31 (2006) 1332-40.

- [2]. R.W. Schefer, W.G. Houf, T.C. Williams, B. Bourne, J. Colton, *Int. J Hydrogen Energ.* 32 (2007) 2081-93.
- [3]. A.D. Birch, D. J. Hughes, F. Swaffield, *Combust. Sci. Technol.* 52 (1987) 161-71.
- [4]. A. Molina, R.W. Schefer, W.G. Houf, *Proc. Combust. Inst.* 31 (2007) 2565-72.
- [5]. S.R. Turns, F.H. Myhr, *Combust. Flame* 87 (1991) 319-35.
- [6]. L.S. Rothman, I.E. Gordon, R.J. Barber, H. Dothe, R.R. Gamache, A. Goldman, V.I. Perevalov, S.A. Tashkun, J. Tennyson, *J. Quant. Spectrosc. Radiat. Transf.* 111 (2010) 2139-50.
- [7]. M.F. Modest, D.C. Haworth, *Radiative Heat Transfer in Turbulent Combustion Systems: Theory and Applications*, Springer, 2016.
- [8]. J.L. Consalvi, F. Nmira, D. Burot, *Combust. Theor. Model.* 20 (2016) 221-57.
- [9]. J.L. Consalvi, F. Nmira, *Fuel* 178 (2016) 37-48.
- [10]. S.L. Brennan, D.V. Makarov, V. Molkov, *J. Loss Prevention Process Indust.* 22 (2009) 353-59.
- [11]. C.J. Wang, J.X. Wen, Z.B. Chen, S. Dembele, *Int. J. Hydrogen Ener.* 39 (2014) 20560-69.
- [12]. M.P. Burke, M. Chaos, Y. Ju, F.L. Dryer, S.J. Klippenstein, *Int. J. Chem. Kin.* 44 (2011) 444-74.
- [13]. Z. Qin, V.V. Lissianski, H. Yang, W.C. Gardiner, S.G. Scott SG, H. Wang, *Proc. Combust. Inst.* 28 (2000) 1663-69.
- [14]. R.P. Lindstedt, in: Bockhorn H (Eds.), *Soot Formation in Combustion: Mechanism and Models*, Springer-Verlag, Berlin, 1994, p. 417.
- [15]. H. Chu, J.L. Consalvi, M. Gu, F. Liu, *J. Quant. Spectrosc. Radiat. Transf.* 197 (2017) 12-25.
- [16]. M.F. Modest, R.J. Riazzi, *J. Quant. Spectrosc. Radiat. Transf.* 90 (2005) 169-89.

- [17]. E.H. Chui, G.D. Raithby, P.M.J. Hughes, *J. Thermophys. Heat Transf.* 6 (1992) 605-11.
- [18]. J.L. Consalvi, F. Nmira, *J. Quant. Spectrosc. Radiat. Transf.* 201 (2017) 1-9.
- [19]. L. Valiño, *Flow Turb. Combust.* 29 (1998) 2139-46.
- [20]. R.S. Barlow, C.D. Carter, *Combust. Flame* 97 (1994) 261-80.
- [21]. R.S. Barlow, N.S.A Smith, J.Y. Chen, R.W. Bilger, *Combust. Flame* 117 (1999) 4-31.
- [22]. W.G. Houf, G.H. Evans, R.W. Schefer, *Int. J. Hydrogen Energ.* 34 (2009) 5961-69.
- [23]. Y.R. Sivathanu, J.P. Gore, *Combust. Flame* 94 (1993) 265-70.
- [24]. A. Wang, M.F. Modest, D. C. Haworth, L. Wang, *J. Quant. Spectrosc. Radiat. Transf.* 109 (2008) 269-79.
- [25]. J. De Ris, *Proc. Combust. Inst.* 17 (1979) 1003-16

## List of table and figure captions

**Table 1.** Flame conditions. For the large-scale H<sub>2</sub> flames, the values in parenthesis are relative to injection through the notional nozzle.

**Table 2.** Emission fractions of the computed flames.

**Figure 1.** Large-scale flame length as a function of time. The experimental data are taken from Schefer et al. [2].

**Figure 2.** Axial and radial profiles of mean and fluctuation of temperature and H<sub>2</sub>O mole fraction. Lab-scale experimental data are taken from Barlow et al. [20] whereas large-scale experimental data are taken from the experiments of Schefer et al. [1] as reported by Houf et al. [22].

**Figure 3.** Radiant fraction as a function of the residence time. The experimental data are taken from Barlow et al. [21] (○), Schefer et al. [1] (◇), and [2] (□ and Δ).

**Figure 4.** Normalized radiative flux at a distance  $R = L_f/2$  as a function of  $z/L_f$ . The experimental data are taken from Sivathanu and Gore [23] and Schefer et al. [1, 2].

**Figure 5.** Effects of TRI on radiant fraction. Data are relative to the simulations of the experiments of Barlow et al. [21] (○), Schefer et al. [1] (◇), and [2] (□ and Δ).

**Figure 6.** Computed  $\chi_{em}$  as a function of  $\beta = \tau_G E_{m,ref}$ . Same legend as in Fig. 5.

**Figure 7.** Computed  $\dot{Q}_{abs}/\dot{Q}_{em}$  as a function of  $\kappa_{p,ref} W_f$ . Same legend as in Fig. 5.

**Figure 8.** Experimental radiant fraction as a function of  $\gamma$ . Same legend as in Fig. 5.